Spin-entropy induced thermopower and spin-blockade effect in CoO

Devendra Singh Negi,[1,*] Deobrat Singh,[2,†] Peter A. van Aken,[1] and R. Ahuja[2,3]

[1]*Stuttgart Center for Electron Microscopy, Max Planck Institute for Solid State Research, Heisenbergstr. 1, 70569 Stuttgart, Germany*

[2]*Condensed Matter Theory Group, Department of Physics and Astronomy, Uppsala University, Box 516, 77120, Uppsala, Sweden*

[3]*Applied Materials, Department of Materials and Engineering, Royal Institute of Technology (KTH), S-100 44 Stockholm, Sweden*

(Received 18 July 2019; published 30 October 2019)

We report spin-entropy-induced thermopower and the occurrence of a spin-blockade effect in stoichiometric disordered CoO. Cation defect-driven distortion in the octahedral ligand field of CoO leads to a charge transfer process and favors the stabilization of Co^{+3} charge states at defect adjacent atomic sites. Moreover, a higher extent of local stoichiometric disruption triggers the spin crossover and magnetic collapse into a Co^{+3} state. Degenerated spin-orbital states on vacancy neighbored atomic sites render the spin-orbital degeneracy to enhance the thermopower in CoO. Furthermore, we unravel an operating spin-blockade effect in CoO. The localized combination of active magnetic states—high-spin Co^{+2} and neutral magnetic states—low-spin Co^{+3} on alternate atomic sites suppress the charge carrier hopping due to a spin blockade. In the pursuit of efficient thermoelectric material, the present investigation explores the potential of the recipe of spin entropy and defect-engineered CoO.

DOI: 10.1103/PhysRevB.100.144108

I. INTRODUCTION

Thermoelectric (TE) materials are considered promising materials for global waste heat management due to their functionality of converting waste heat energy into electricity. Furthermore, in pursuit of sustainable and fossil-free green-energy resources and energy scavenging, recently TE materials have also gained substantial attention [1–6]. The efficiency of a TE material is generally quantified by a dimensionless quantity known as figure of merit (ZT). ZT proportionally depends on the Seebeck coefficient (S), electrical conductivity (σ), temperature (T), and is also inverse proportional to the total thermal conductivity (K); [$ZT = \frac{S^2\sigma}{K}T$]. To raise the efficiency of TE material, mutual optimization of these interdependent properties poses a grand challenge and remains a key issue. Various strategies including, nano-structuring [7–10], defect engineering [11–13], rattling ion [14–16], spin-orbital degeneracy [17–20], band convergence [21–23], and bond anharmonicity [24–26] are currently being explored to raise the efficiency of TE materials. However, currently the highest ZT is reported to be ∼2.6 [25], whereas it is suggested that ZT needs to be in the range of ∼3–4 to be comparable with other energy-harvesting methods, e.g., wind and solar energy [27]. In the search for efficient TE materials, transition metal oxides (TMOs) have attracted wider attention due to their high temperature stability, abundance, and tunable electrical and thermal properties [5,28–30]. Moreover, the dependent parameters of ZT, i.e., σ and K, are closely associated with spin, orbital, and lattice degrees of freedom. Therefore, TMOs offers potential possibilities to tailor the ZT and have emerged as one of the viable candidates for efficient TE materials [27]. Various erstwhile investigations had explored the influence of strong electron-electron correlations, spin-orbital degeneracy on the thermopower. It is generally considered that a subtle interplay of spin-orbital degeneracy and strong electron-electron correlations leads to the high thermopower in strongly correlated materials. For instance, the large thermopower in the strongly correlated material $NaCoO_2$ was attributed to the spin-orbital degeneracy, which eventually stems from a combination of magnetically active high-spin (HS) $-$ Co^{+4} states and nonmagnetic low-spin (LS) $-$ Co^{+3} states on the adjacent atomic sites. Spin-entropy induced by the combination of HS-LS on adjacent atomic sites serves as a key ingredient for raising the thermal efficiency of $NaCoO_2$. Focusing on spin-orbital degeneracy, cobaltates offer a promising pathway to engineer the thermal efficiency of TE materials. Cobaltates exhibit distinct spin and orbital degrees of freedom which essentially provide a fertile ground for tuning the spin-entropy contribution to engineer the efficiency of TE materials [30–33]. In cobaltates, the Co ion exhibits distinct charges (Co^{+2}, Co^{+3}, Co^{+4}), spins [HS, LS, and intermediate spin (IS)], and orbital degrees of freedom. In cobaltates, the trivalent Co^{+3} state is especially quite intriguing, since this charge state demonstrates various spin degrees of freedom, i.e., (HS $[(\uparrow 3\,t_{2g}\downarrow 1\,t_{2g})(\uparrow 2\,e_g)[S=2]]$), (LS $[(\uparrow 3\,t_{2g}\downarrow 3\,t_{2g})$ $[S=0]]$) and (IS $[(\uparrow 3\,t_{2g}\downarrow 2\,t_{2g})(\uparrow 1\,e_g)[S=1]]$). The spin state in cobaltate and other TMOs is dictated by the mutual complex interplay of the crystal-field-splitting energy, multiplet effects, Hund's exchange, band hybridization, etc. Various cobaltate materials have shown their potential to be utilized as an efficient TE material. Therefore, owing to the tunable spin and charge degree of freedom, cobaltate naturally draws attention to be explored in the pursuit of efficient TE materials [34,35]. Apart from the spin-orbital degeneracy contribution, defect engineering is also considered as a versatile approach to enhance ZT. Defects in TE materials can enhance phonon scattering, which subsequently reduces the thermal conductivity [12,36–40]. Moreover, a local stoichiometric

*D.Negi@fkf.mpg.de

†deobrat.singh@physics.uu.se

disruption in TMOs is often capable to introduce a stark influence on localized states [41,42]. Designing a functional defect in TMOs is also considered as a novice approach to introduce functionalities in strongly correlated materials [43,44].

In the present paper, we computationally establish that stoichiometric disordering induces the spin-orbital degeneracy in CoO, which subsequently enhances the thermal efficiency. In Sec. III A, we study the spin crossover in nonstoichiometric CoO. Section III B further explores the ramification of the magnetic collapse on Co^{+3} in CoO, and investigates the thermopower in nonstoichiometric CoO. Finally, based on the charge transport, Sec. III C unravels the operating spin-blockade effect in CoO.

II. COMPUTATIONAL METHOD

First-principles electronic-structure calculations were executed by utilizing WIEN2K code [45]. WIEN2K is full-potential linear augmented plane wave plus local-orbital-based method for density-functional theory (DFT) calculations. The AFM-II-type magnetic structure of CoO is considered for all calculations. Stoichiometric disruption in CoO is simulated by implanting a single Co vacancy in the unit cell and a $(2 \times 2 \times 2)$ supercell of CoO, containing a total of 48 atoms, respectively [42,46]. Resultant distorted structural configurations were further fully relaxed with the convergence criteria of charge ($0.001e^-$), energy (0.0001 Ry), and force (1 mRy/a.u.) convergence with the generalized gradient approximation (GGA)-Perdew-Burke-Ernzerhof (PBE) exchange correlation functional. The relaxed lattice parameters are obtained as $a = 3.08$ Å, $c = 14.95$ Å and $a = 5.88$ Å, $c = 26.99$ Å for $V_{Co} = 16.6\%$ and $V_{Co} = 4.16\%$, respectively. DFT calculations were carried out by separating the valence and core states by -6 Ry. Spin-polarized self-consistent field cycle calculations were carried out with 3000 K points in the first Brillouin zone. In the simulation study, the $R_{MT}K_{Max}$ parameter was set to 7. The GGA exchange correlation functional often underestimates the band gap for strongly correlated systems [47]. Therefore, to carry out the band-gap correction, calculations were performed with the modified Becke-Johnson method and were also compared with GGA + U method, respectively [48]. A self-interaction correction scheme is employed for LDA + U-based calculations [49]. On-site interaction of Co $- 3d$ states are considered with a Hubbard potential U = 7.1 eV and a local exchange interaction with $J = 1$ eV, respectively [41]. The BoltzTraP code is utilized for calculating the temperature-dependent thermopower and transport functions within the Boltzmann transport theory under a constant-scattering-time approximation [50]. In the Boltzmann transport formalism, σ, S, and the electronic part of the thermal conductivity (k_e) are expressed as

$$\sigma(T,\mu_i) = q_e^2 \int_{E_0}^{\infty} \Xi(E)\left(-\frac{\delta f(E,\mu_i,T)}{\delta E}\right)dE, \quad (1)$$

$$S(T,\mu_i) = \frac{q_e k_B}{\sigma}\int_{E_0}^{\infty}\Xi(E)\left(-\frac{\delta f(E,\mu_i,T)}{\delta E}\right) \times \left(\frac{E-\mu_i}{k_B T}\right)dE, \quad (2)$$

$$\kappa_0(T,\mu_i) = k_B^2 T\int_{E_0}^{\infty}\Xi(E)\left(-\frac{\delta f(E,\mu_i,T)}{\delta E}\right)\left(\frac{E-\mu_i}{k_B T}\right)^2 dE, \quad (3)$$

$$\kappa_e = \kappa_0 - T\sigma S^2, \quad (4)$$

where q_e represents the elementary charge, $f(E,\mu_i,T)$ is the Fermi distribution function at a given temperature T, μ_i is the chemical potential and $\Xi(E)$ is the transport distribution function, which is a function of carrier energy E and is defined by

$$\Xi(E) = \sum_{i,\mathbf{k}} \tau_{i,\mathbf{k}}(E)\upsilon_\alpha(i,\mathbf{k})\upsilon_\beta(i,\mathbf{k})\delta(E - E_{i,\mathbf{k}}), \quad (5)$$

where i represents the band index, $\mathbf{k}$ is the k-point, $\tau_{i,\mathbf{k}}(E)$ and $\upsilon_\alpha(i,\mathbf{k})$ are the electron relaxation time and αth the component of the group velocity $v(i,\mathbf{k})$. Equations (1)–(4) are used to calculate the TE properties of CoO. It is noteworthy here that, in the present investigation, we have calculated the electronic figure of merit,

$$ZT_e = \frac{\sigma S^2}{K_e}T, \quad (6)$$

which reflects the electron transport characteristics and provides an upper bound of the total ZT.

III. RESULTS AND DISCUSSION

A. Spin crossover in nonstoichiometric CoO

This section investigates the influence of the local stoichiometric disorder on the charge and magnetic states of Co atoms, residing on the local vicinity of a defect site. CoO is a strongly correlated material and crystallizes in the NaCl-type rock-salt structure [51]. It is a charge-transfer antiferromagnetic insulator. The Neel temperature of CoO is reported to be 291 K [52]. CoO exhibits an AFM-II magnetic structure, in which the magnetic moments stack antiparallel along alternative (111) planes [52]. Previous theoretical investigations have suggested that a localized cation deficiency in CoO evinces a stark influence on the local charge distribution [41]. However, experimental realization of defect-induced spin-ordering and periodic lattice distortion in CoO is reported as well [53,54]. Thus, both theoretical and experimental investigation advocates the strong effect of nonstoichiometry on electron correlations in CoO. It is noteworthy here that defects inherently do exist in all materials and for CoO such defect densities lie in the range of 0.3–3 % at ambient conditions [55]. Furthermore, the formation of cation deficiency V_{Co} is also suggested as energetically favorable over anion deficiency [53]. We evaluate the relative stability of nonstoichiometric structures by computing the cohesive energy and compare with stoichiometric CoO. Cohesive energy of CoO, $V_{Co} = 16.6\%$, and $V_{Co} = 4.16\%$ is 5.92 eV/atom, 5.98 eV/atom, and 5.99 eV/atom, respectively. A relatively small difference in cohesive energy ($\sim$0.07 eV/atom) between CoO and $V_{Co} = 4.16\%$ indicates the formation of cation vacancy is favorable in CoO. However, the cohesive energy of O vacancy ($V_O = 16.6\%$) is found to be 5.85 eV/atom. Cohesive energy indicates the favorable

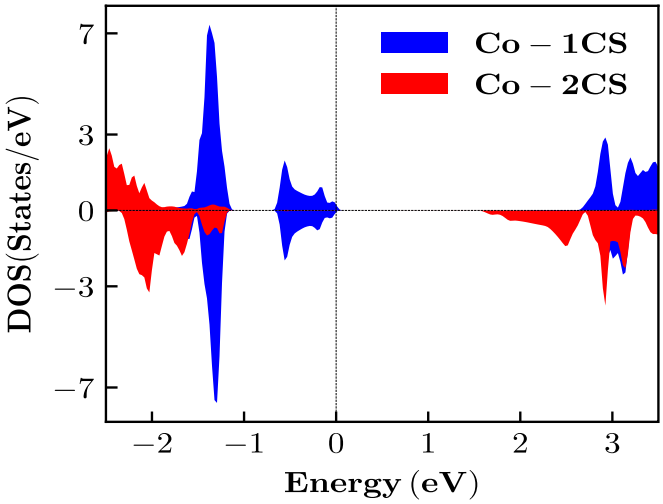

FIG. 1. Spin crossover in non-toichiometric CoO ($V_{Co} = 16.6\%$). Magnetic neutral states LS − Co^{+3} are formed on the adjacent defect atomic sites.

formation of V_{Co} over V_O. Recently, we have also computationally demonstrated the defect-induced half metallicity in CoO [42]. In CoO, the Co-O bond is polarized and the electronegativity of the oxygen (O) atom is ∼1.8 times to the Co atom. Therefore, introducing a local V_{Co} allows the O atom to allure the electronic charge from the nearest atomic site. Defect-generated hole states in the O atom are compensated by a charge transfer process. Resultant charge inflow toward the O atoms transforms the defect adjacent Co^{+2} cation atom to a higher Co^{+3} valence state [41,42,56] (see Fig. 3).

Figures 1 and 2 show the spin-polarized density of states (DOS) of the Co-*d* state located in the vicinity (1CS) of a V_{Co}, and at far distant in the second coordination shell (2CS), with higher ($V_{Co} = 16.6\%$) and lower ($V_{Co} = 4.16\%$) defect densities, respectively. Although, in the earlier case, the defect

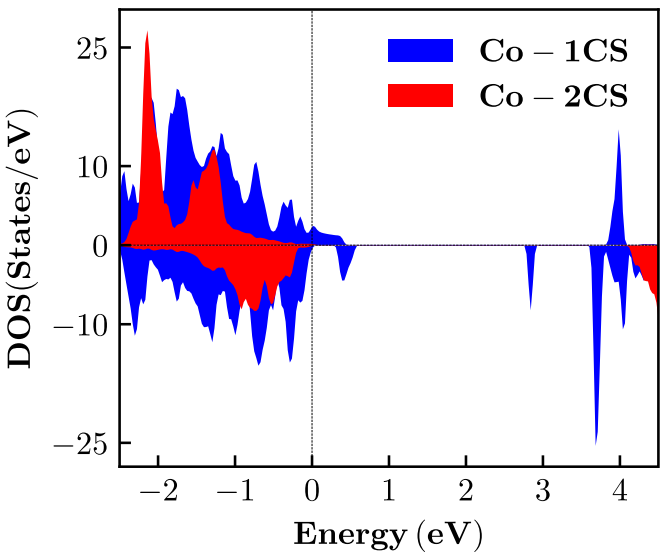

FIG. 2. DOS profile of Co atom located in 1CS, 2CS from V_{Co} with $V_{Co} = 4.16\%$. The half-metallic state can be observed at a vacancy-neighbored atom.

density seems to be high, the existence of high defect density in TMOs was affirmed to be prerequisite for magnetic percolation [57]. For $V_{Co} = 16.6\%$, Co atoms located adjacent to V_{Co} show a nearly symmetric DOS distribution in both spin channels, i.e., spin up and spin down, in the valence band. A symmetric valence band distribution of the DOS indicates an equal charge distribution in Co − 3*d* orbital spin-up and spin-down channels, respectively. Equal charge distribution in both spin channels also indicates the magnetic dead state of the defect adjacent atom. However, Co atoms residing at the second CS from the V_{Co} retains the magnetic nature and represents asymmetric states in the spin channels. Furthermore, we notice that in comparison to the 2CS Co atom, the available energy states at the Fermi level (E_F) are profoundly enhanced on the Co atom in the 1CS. It is noteworthy here that the thermopower is proportional to the DOS at Fermi level [27]. We will discuss the effect of enhanced energy states at E_F on the thermopower in Sec. III B. Lower defect density does not introduce a nonmagnetic atom in the defect neighboring site; however, an increased energy level can be noticed (Fig. 2). On defect adjacent atomic sites, a strong hybridization of Co-*d*-O-*p* leads to the half metallicity [42]. Therefore, enhanced states on vacancy neighboring atomic sites also stretch beyond the Fermi level. In comparison to the higher stoichiometric disruption, the DOS remains nearly equal on the defect adjacent atom as well as on the far-distance Co atoms. DOS calculations indicate that the higher extent of stoichiometric disruption do trigger the magnetic collapse into a Co^{+3} state, located at the vicinity of the defect plane. The existence of a LS state indicates that at higher stoichiometric disorder the crystal field stabilization energy (Δ_{cf}) dominates the Hund's coupling. However, the density of $V_{Co} = 4.16\%$ yet favors the magnetically active ionic state. Interestingly, apart from the chemical pressure, various erstwhile investigations have shown that the magnetic collapse in CoO can also be induced by the mean of external physical pressure [58–60].

Furthermore, we rationalize the spin-state of a Co atom in the neighborhood of a vacancy by computing the electronic charge and magnetic moment distribution. For $V_{Co} = 16.6\%$, the Co atom adjacent to V_{Co} exhibits ∼3/3 electrons in spin-up and spin-down channels, respectively. Equal charge distribution in both spin channels suggests a magnetic dead state and congruently reinforces the symmetric energy states distribution as shown in Fig. 1. The Co atom further away from the V_{Co} shows a stoichiometric-type electron-charge distribution in the Co − 3*d* orbitals, i.e., ∼4/2 electrons in spin-up and spin-down channels, respectively. In agreement with the DOS, electron distribution in spin-up and spin-down channels, we obtain a nearly magnetically inert Co state at the defect adjacent site. The Co atom located in the vicinity of the V_{Co} magnetically collapses and shows a magnetic moment value of ∼0.00 μB, whereas the Co atom located at 2CS retains its magnetic nature, akin to stoichiometric CoO. The Co atom at 2CS demonstrates the magnetic moment to be ∼2.72 μB. Thus, with lower extent of stoichiometric disordering, Hund's coupling dominates Δ_{cf} and no magnetic collapse at the defect adjacent Co atom is observed. However, the existence of a higher charge state (Co^{+3}) on the defect adjacent atomic site is noted with both defect densities. The local stoichiometric disruption distorts the local octahedral

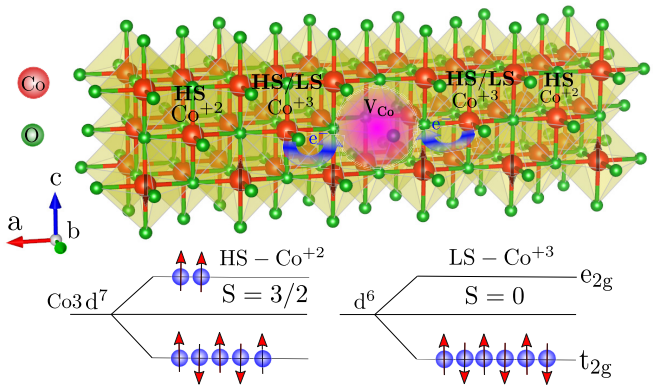

FIG. 3. Schematic representation of the ramification of stoichiometry disordering in CoO. Modification of charge and spin-state of a defect adjacent Co atom occurs due to a charge transfer process.

ligand field in CoO and, therefore, the magnetic collapse and the spin crossover in Co^{+3} state is certainly susceptible to the complex interplay of the competing and modified crystal field and Hund's rule coupling. Moreover, on the ground of energetically stability, various previous investigations had established that the spin HS-LS configuration on adjacent atomic sites is energetically favorable than other possible spin configurations in cobaltates. Spin-crossover associated to the lattice distortion is also reported [61]. Based on the above DOS profile analysis, we construct a schematic figure, which illustrates the ramification of the local stoichiometric disordering in CoO (Fig. 3). In Fig. 3, V_{Co} represents the localized Co deficiency and the curved arrows indicate the charge transfer process toward higher electronegative O atoms. The spin state at the defect adjacent atomic site depends on the extent of crystal-field distortion induced by stoichiometric disordering. The defect induced distinct charge and spin-state configuration on adjacent atomic sites will also introduce the spin-orbital degeneracy in the nonstoichiometric CoO system. Therefore, aligning our results with previous explorations, it is tempting to explore whether such generated entropy can lead to the enhancement of the thermopower in CoO. We explore such possibilities in the next section (Sec. III B).

B. Spin-entropy and enhanced thermopower in CoO

In the previous section, Sec. III A, we have deduced that V_{Co} in CoO introduces a higher charge state Co^{+3}. An additional higher charge state HS/LS $- Co^{+3}$ coexisting with the HS $- Co^{+2}$ state will also introduce a spin-entropy in the system. Therefore, having a system in hand with distinct charge and spin configurations encourages us to investigate the spin-orbital-degeneracy-induced thermopower in CoO.

It is well known, that the spin entropy acts as the main source for the large thermopower in any cobaltate system [18,19,62–66]. The spin-entropy contribution to the thermopower is strongly related with the spin-entropy current and the population of free spins inside the systems [30], which depends largely on the higher charge concentration with respect to lower charge state and the degeneracy of the Co ions [29]. For instance, in $Ca_3Co_4O_{9+\delta}$ it was deduced that the spin-orbital degeneracy introduced by Ce doping enhances

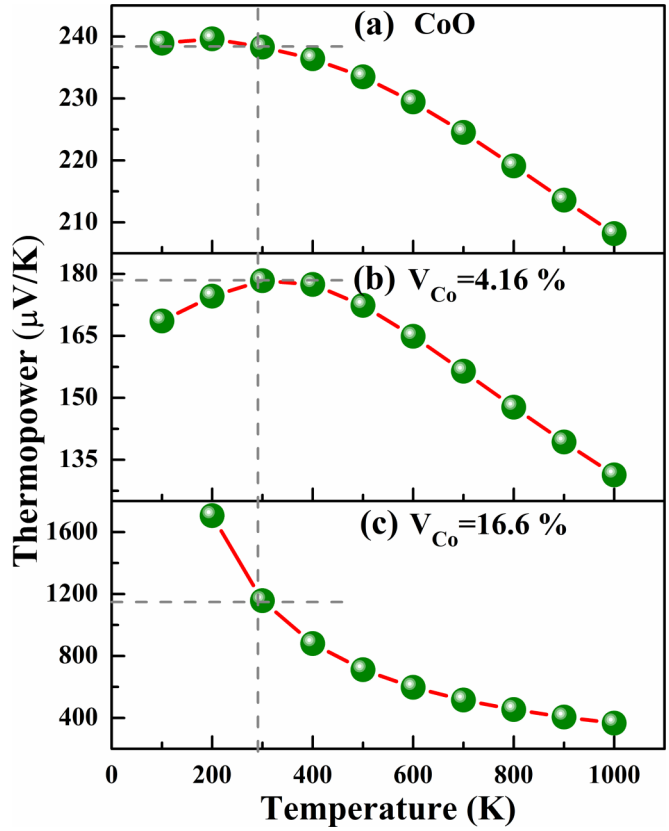

FIG. 4. Variation of thermopower as a function of temperature for (a) stoichiometric CoO and nonstoichiomtric CoO structures with (b) $V_{Co} = 4.16\%$ and (c) $V_{Co} = 16.6\%$. The vertical dashed line represents the thermopower at Neel temperature. Enhanced spin-entropy in nonstoichiometric CoO ($V_{Co} = 16.6\%$) enhances the thermopower by approximately a factor of 5, compared to stoichiometric CoO.

the thermopower [20]. From this prospective, it provides an understanding of microscopic mechanisms by which external doping affects the spin entropy to enhance the thermopower for TE materials. This further creates a curiosity that the thermopower can be engineered if we introduce a spin-orbit degeneracy by creating a cation deficiency, instead of external doping in the system. Motivated by this curiosity, we introduced a deficiency of the Co atoms in CoO system, which can enhance the spin entropy by introducing an additional charge state Co^{+3} via charge transfer.

Before studying the thermal response of nonstoichiometric CoO, we analyze stoichiometric CoO. The temperature dependence of the thermopower and thermal conductivity of simple rock-salt CoO is shown in Figs. 4(a) and 6(a), respectively. Generally, the overall shape and magnitude of the thermopower curve can be correlated to the DOS at the Fermi level. At room temperature, the magnitude of thermopower is 238.90 μ V/K, but at the Neel temperature $T_N = 291$ K, the value is found to be 239.62 μ V/K. Above the Neel temperature, the magnitude of the thermopower decreases with increasing temperature, where the charge carriers dominate the thermal and electrical conductivity. This is presented in Figs. 6(a) and 9(a), suggesting that our computed results are

consistent with previous reported theoretical calculations [67]. Consistently, Bruck and Tannhauser also have reported the reduction in the thermopower at $T_N = 291$ K [56]. Generally, the thermopower is proportional to the electric field that occurs because of the diffusion of electric charge carriers from the hot side to the cold side of the material as a result of a temperature gradient in the materials. Therefore, S can be expressed as, $S = E/\nabla T$, where E and ∇T are the electric field and temperature gradient. For strongly correlated materials, the thermopower at higher temperature is generally quantified by the Heikes formula [29]. Heikes formula accounts for both spin and orbital degeneracy to calculate the thermopower and generally is expressed as

$$S = -\frac{k_B}{e}\ln\left(\frac{g_2}{g_3}\frac{x}{1-x}\right), \tag{7}$$

where g_2, g_3, and x denote the electronic degeneracy terms for the electron donors Co^{+2}, electron acceptors Co^{+3}, and the fraction of electron acceptors, respectively [68]. Based on Eq. (1), we can calculate the total spin entropy for the high-temperature limit using the estimated Co^{+3} concentration. Figure 3 shows that the spin entropy is enhanced by the deficiency of Co atoms in the CoO system. According to Heikes formula, the thermopower in cobalt oxide was found to be 214 μV/K [29], which is consistent with our result. At higher temperature around 1000 K, the thermopower is of the order of 200 μV/K, which is a typical magnitude for the thermopower of conventional semiconductors. This is consistent with the fact that majorly Co^{+2} ions become itinerant at higher temperature. As discussed before, stoichiomtric CoO have antiferromagnetic behavior. Also, the coupling of charge and spin degrees of freedom is an intrinsic character for materials with strongly correlated electrons. It is well known that the antiferromagnetic ordering suppresses electron hopping and reduces the kinetic or band energy. The variation of the electrical conductivity up to the Neel temperature is much less due to the suppression of electron hopping and thermopower is inversely proportional to electrical conductivity [see Eq. (2)]. Therefore, in such temperature regime (below the Neel temperature $T_N = 291$ K), the thermopower has nearly constant values. Moreover, it is also known that above the Neel temperature, the material is typically paramagnetic, which enhances the electrical conductivity and, therefore, a reduced thermopower can be observed above the Neel temperature.

Now we explore the influence of the spin crossover on the thermopower in nonstoichiometric CoO. The temperature-dependent thermopower of nonstoichiometric structures, i.e., $V_{Co} = 4.16\%$ and 16.6% of CoO are depicted in Figs. 4(b) and 4(c), respectively. We found the similar trends of the thermopower in nonstoichiometric CoO stucture with $V_{Co} = 4.16\%$ akin to stoichiometric CoO. Section III A unravelled that with stoichiometric disordering in $V_{Co} = 4.16\%$, two distinct charge states, i.e., Co^{2+} and Co^{3+} coexists. Such a distinct charge state further introduces the spin entropy in the system. Furthermore, the appearance of the excess charge carrier also affects the thermopower and it strongly depends on electronic correlations and large configurational entropy [69]. Figure 4(b) shows that at lower temperature (300 K), the thermopower for $V_{Co} = 4.16\%$ is 179.25 μV/K, which is slightly lower than the stoichiometric CoO at the same temperature. Although an enhanced thermal response is expected due the additional spin entropy in $V_{Co} = 4.16\%$, yet a reduced thermopower response is observed. Moreover, from Fig. 2 it is evident that at $V_{Co} = 4.16\%$, CoO exhibits a half-metallic nature [42]. Therefore, the enhanced metallic nature with spin-up charge carriers are responsible for reducing the thermal response in $V_{Co} = 4.16\%$. Further reduction above the Neel temperature can be expected due to the suppression of antiferromagnetic ordering and excess population of itinerant charge carriers. Moreover, as compared to stoichiometric CoO, we observed a higher response (~5 times) in thermopower with stoichiometric disordering of $V_{Co} = 16.6\%$ [see Fig. 4(c)]. Near the Neel temperature, we obtain the thermopower as 1157 μV/K [Fig. 4(c)]. At $V_{Co} = 16.6\%$ in stoichiometric CoO, we found the large DOS or flat bands at the Fermi level is one of the reasons to enhance the thermopower, which increases the effective mass value, and thermopower is directly proportional to effective mass and carrier mobility is inversely proportional to effective mass [70,71] (see the detailed descriptions in Ref. [49]). Our thermopower results indicate that $V_{Co} = 16.6\%$ largely enhances the spin entropy, implying that the enhanced thermopower originates mainly from a spin-entropy enhancement. Additionally, a large and positive thermopower in nonstoichiometric CoO ($V_{Co} = 16.6\%$) at low temperature indicates the possibility of a spin blockade [72], which will be discussed in detail in Sec. III C.

Furthermore, we have also computed the anisotropic behavior of the thermopower, as shown in Fig. 5. We observe isotropic behavior below the Neel temperature (291 K) in stoichiometric CoO structure. At higher temperatures above $T_N = 291$ K, it starts to exhibits an anisotropic response. This is consistent with the fact that the Co^{2+} ions become itinerant. Therefore, a higher anisotropic response can be expected with stoichiometric disordering. The behavior of the directional components of the thermopower at a low defect density $V_{Co} = 4.16\%$ is just opposite as compared to stoichiometric CoO structure [Fig. 5(b)]. Such type of anisotropic behavior can be expected due to the induced half-metallic nature in $V_{Co} = 4.16\%$. In this case, at Fermi level we find a single spin channel dominated by spin-up population. The anisotropic component S_{xx} dominates the S_{zz}. The S_{xx} component of the thermopower has higher values as compared to S_{zz} at lower temperatures, while the thermopower in the S_{zz} direction shows increasing order up to 500 K. Additionally, with $V_{Co} = 16.6\%$, the directional component of the thermopower shows an isotropic behavior at large thermopower. The isotropic thermopower response in $V_{Co} = 16.6\%$ is quite resistant to the thermal agitation.

The thermal conductivity is also an important parameter for TE materials; therefore, we have also computed the thermal conductivity response as a function of temperature and compared stoichiometric CoO and other nonstoichiometric structures at constant relaxation time $\tau \approx 10^{-14}$ s (see Fig. 6). The thermal conductivity (K) comprises the contributions from the lattice (phonon scattering) and conductive carriers (κ_e). It is noteworthy here that, in the present computational study, we have only considered the κ_e contribution to the thermal conductivity. A previous experimental study reports the thermal conductivity of stoichiometric CoO at 300 K as

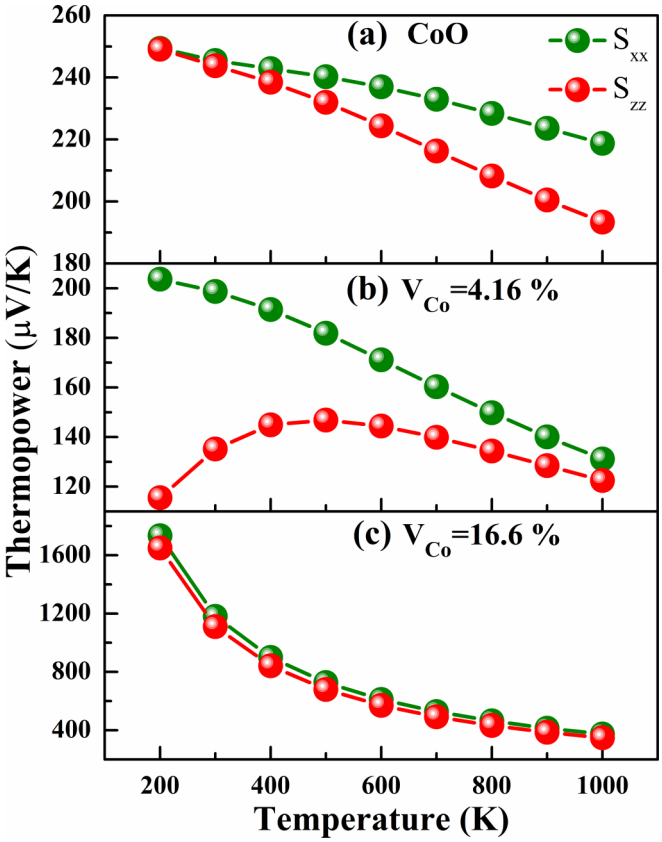

FIG. 5. Variation of anisotropic thermopower as a function of temperature for (a) stoichiometric CoO and nonstoichiomtric CoO structures with (b) $V_{Co} = 4.16\%$ and (c) $V_{Co} = 16.6\%$. The green and red colors denote the thermopower in the in-plane (xx) and out-of-plane (zz) direction.

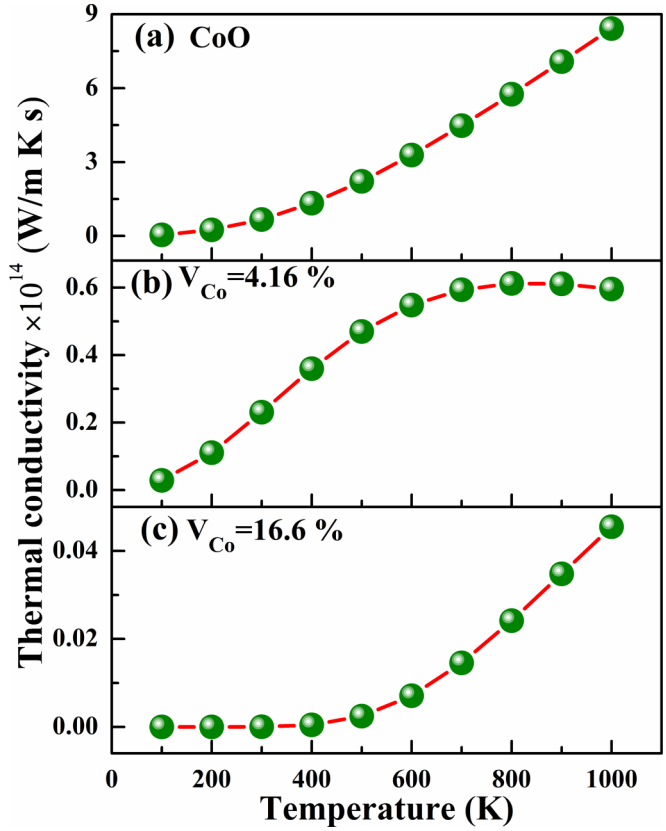

FIG. 6. Variation of thermal conductivity as a function of temperature with a constant relaxation time ($\tau = 10^{-14}$ s) for (a) stoichiometric CoO and nonstoichiomtric CoO structures with (b) $V_{Co} = 4.16\%$ and (c) $V_{Co} = 16.6\%$. The thermal conductivity at $V_{Co} = 16.6\%$ in nonstoichiomtric CoO is considerably reduced due to the presence of spin entropy.

$\sim$20 $Wm^{-1}k^{-1}$ [73]. If the electron conduction is due to one type of charge carrier, then κ_e can be estimated by the Wiedemann–Franz law. Thermal conductivity proportionally depends on the conductive carrier, therefore below the Neel temperature, due to the antiferromagnetic ordering we observe a reduced K [Fig. 6(a)]. However, increasing the temperature, the conductive charge carriers (Co^{2+}) become itinerant and the thermal conductivity increases almost linearly. The directional-dependent thermal conductivity does not exhibit any anisotropic nature below the Neel temperature (291 K). However, beyond the the Neel temperature an anisotropic nature gradually emerges in the thermal conductivity components, i.e., in in-plane κ_{xx} and out-of-plane κ_{zz} directions. The observed emergence of anisotropy in thermal conductivity can again be correlated to the suppression of antiferromagnetic ordering at higher temperature.

Now we discuss the effect of nonstoichiometry on thermal conductivity as represented in Figs. 6(b) and 6(c), respectively. The thermal conductivity of nonstoichiometric CoO increases as temperature increases, whereas the magnitude of the thermal conductivity reduces in nonstoichiometric structures compared to the stoichiometric structure due to increased phonon scattering by a certain defect density. This is a consequence of the mixed ionic states of Co^{2+} and Co^{3+} cobalt ions presented in Fig. 3. The decrease in the thermal conductivity is highly desirable for potential applications of TE materials. Recently, it has been reported that some cobaltate systems doped with Fe and Ni exhibit dramatic reduction of the thermal conductivity compared to stoichiometric CoO materials and further leads to a significant improvement of the figure of merit [69]. Moreover, in our present paper, the chemical approach includes the creation of Co deficiency to enhance the spin-orbit degeneracy and to reduce the thermal conductivity. The lower extent of stoichiometric disordering ($V_{Co} = 4.16\%$) exhibits increasing thermal conductivity with increasing the temperature. In general, the thermal conductivity decreases upon increasing the defect density [74]. Therefore, a reduced magnitude of the thermal conductivity is observed. Increased thermal conductivity at elevated temperature can be expected due to the increased itinerant charge carrier. Higher thermal anisotropy is also observed for $V_{Co} = 4.16\%$. The thermal conductivity channel K_{xx} dominates the K_{xx} channel ($K_{xx} \sim 10^4 \times K_{zz}$). Higher extent of stoichiometric disordering $V_{Co} = 16.6\%$ exhibits a distinct thermal conductivity response against the temperature. The thermal conductivity is severally suppressed up to the temperature range of $\sim$400 K (K $\sim$ 0). Beyond 400 K, K increases rapidly [Fig. 6(c)]. The anisotropic thermal conductivity response [Fig. 7(c)] unravels that the increment

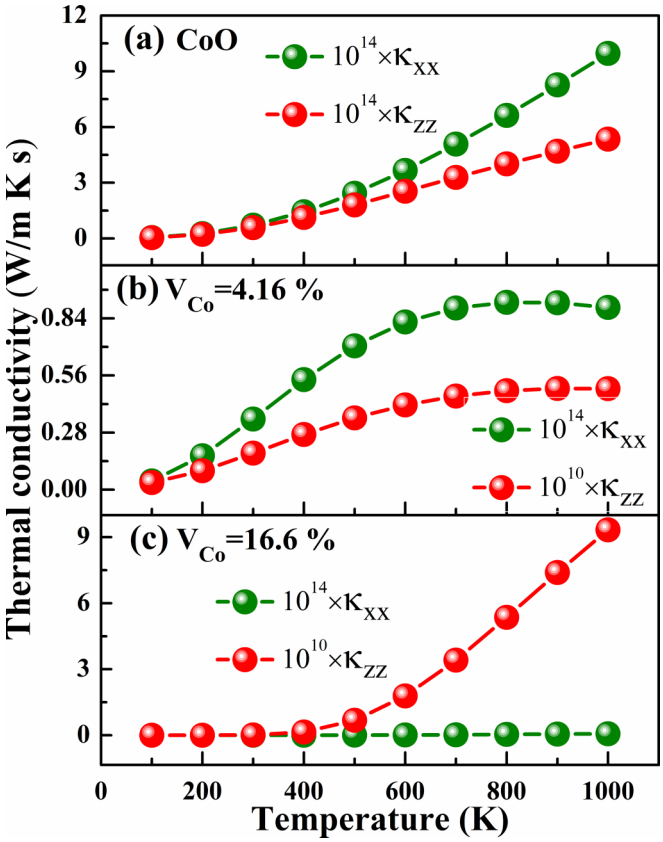

FIG. 7. Variation of an anisotropic thermal conductivity as a function of temperature with a constant relaxation time ($\tau = 10^{-14}$ s) for (a) stoichiometric CoO and nonstoichiometric CoO structures with (b) $V_{Co} = 4.16\%$ and (c) $V_{Co} = 4.16\%$. The green and red colors denote the thermal conductivity in the in-plane (xx) and out-of-plane (zz) direction. An abrupt reduction of the thermal conductivity in the out-of-plane direction for $V_{Co} = 16.6\%$ is observed.

with increasing temperature occurs only in the K_{zz} channel. However, the conductivity channel K_{xx} nearly vanishes in all temperature regimes. This distinct anisotropic response along the K_{xx} channel can be correlated to the HS-LS spin configuration and subsequent spin blockade. The spin-blockade-assisted enhancement of the thermopower is also reported [72]. The spin blockade in CoO is discussed in Sec. III C. Ramification of the reduced thermal conductivity reflects in the increment of power factor scaled by constant relaxation time ($\tau = 10^{-14}$ s) and the electronic figure of merit ZT_e of nonstoichiometric CoO. Here, we have computed only electronic part of thermal conductivity κ_e. However, having lattice contribution to thermal conductivity may reduce ZT value by an order of magnitude. Therefore, additional studies which include lattice thermal conductivity are necessary to estimate the TE performance of CoO. Our computed results shows that at 300 K, $ZT_e(V_{Co} = 16.6\%) \sim 1.9$. Additional information about the electronic structures, power factor, and ZT_e can be obtained in Ref. [49].

C. Spin-blockade effect in CoO

In the previous section, Sec. III A, we have computationally established that a higher extent of chemical pressure induced via stoichiometric disordering in CoO triggers the magnetic collapse on defect adjacent Co^{+3} charge state and favors the $HS - Co^{+2} - LS - Co^{+3}$ spin configuration locally. This section (Sec. III C), further explores the consequence of coexisting magnetic-active HS and magnetic-inert LS states on the charge transport. Stable and coexisting $HS - Co^{+2} - LS - Co^{+3}$ spin configurations on adjacent Co atomic site are also reported in various cobaltate systems [61,75–78]. Moreover, apart from the chemical pressure, external stimulation, e.g., pressure and temperature can also induce such spin crossovers in cobaltate materials [34,58,79–81]. On the ground of energetic stability, a combination of $HS - Co^{+2} - LS - Co^{+3}$ on adjacent atomic sites is advocated stable than other possible spin-state configurations [34,77,82–86]. Interestingly, the relation of spin crossover to metal-to-insulator transition in cobalatates is also reported in few erstwhile investigations [60,84,87]. However, from the perspective of electrical and thermal conductivity, the consequence of such ($HS - Co^{+2} - LS - Co^{+3}$) spin configuration on CoO lacks wide investigations. Therefore, having a system in hand with $HS - Co^{+2} - LS - Co^{+3}$ spin configuration, it is intriguing to explore how such local spin neutrality can influence the charge transport and spin-blockade can eventually be created in simple rock-salt CoO via defect engineering [72,88–90].

The suppression of electron hopping on adjacent atomic sites due to the compulsion to generate the identical spin configuration on adjacent atomic sites is referred to as spin blockade. Figure 8 represents a schematic diagram illustrating the possible spin-blockade effect in CoO. Figure 8 shows the electron spin-configuration of the HS-Co^{+2} and LS-Co^{+3} state on defect adjacent atomic sites (Fig. 3). Charge transport occurs via charge hopping on adjacent atomic sites without altering the spin configuration on native atomic sites. However, the violation of such a condition is known as spin blockade, which often results in introducing higher electrical resistance [88]. Figure 8 signifies that the electron hopping is not permitted from $HS - Co^{+2}$ to $LS - Co^{+3}$ state on adjacent atomic site. The hopping of charge carriers from $HS - Co^{+2}$ to $LS - Co^{+3}$ does not lead to the generation of identical pairs of spin state by the charge interchange on adjacent atomic sites. However, under such conditions, the hopping will result in a distinct spin configuration. Therefore, one cannot interchange HS-LS by hopping a charge on adjacent atomic sites during electron transport. Therefore, the incapability of electron hopping should reflect a drastic reduction of the electron conductivity in CoO. Among cobaltates, the spin blockade is also attributed to the giant magnetoresisitance in $La_{1.5}Sr_{0.5}CoO_4$ and enhanced thermopower in $HoBaCo_2O_{5.5}$ [72,88]. A part of cobaltates' spin-blockade phenomena has also been reported in quantum dot systems [91,92]. Controlling and manipulating the spin crossover and associated spin blockade in cobaltates offers potential possibilities for spintronics applications [93–95].

Next we explore the scenario of the spin-blockade effect in nonstoichiometric CoO, comprising a HS-LS configuration. Figure 9 compares the temperature-dependent electrical conductivity of CoO with other nonstoichiometric structures, i.e., $V_{Co} = 4.16\%$ and 16.6%, respectively, at constant relaxation time $\tau \approx 10^{-14}$ s. The electrical conductivity of

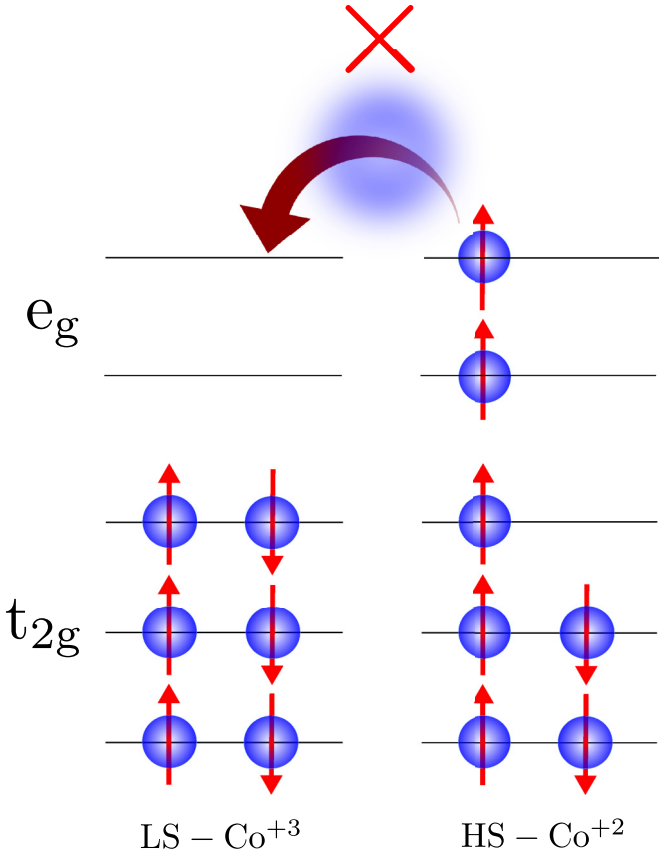

FIG. 8. Schematic illustration of spin blockade in CoO. Charge hopping within adjacent HS − Co^{+2} − LS − Co^{+3} is not permitted due to the operating spin-blockade effect in nonstoichiometric CoO.

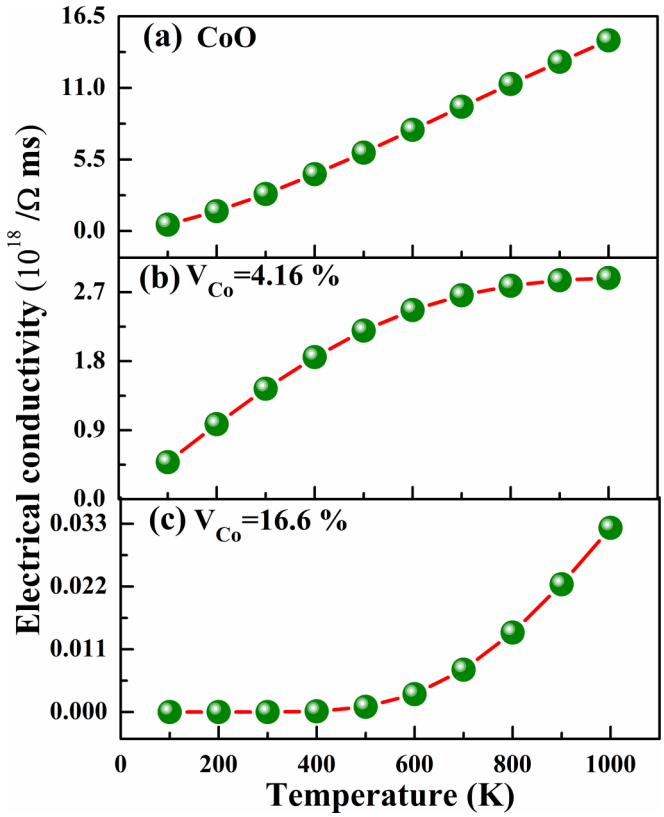

FIG. 9. Variation of electrical conductivity as a function of temperature with a constant relaxation time ($\tau = 10^{-14}$ s) for (a) stoichiometric CoO and (b), (c) nonstoichiomtric CoO, respectively. (c) A significant reduction in the electrical conductivity (σ) is observed with spin-crossover, suggesting the operating spin-blockade effect.

stoichiometric CoO linearly enhances with raising the temperature [56]. It is well known that the antiferromagnetic ordering suppresses the charge hopping on adjacent atomic sites. Therefore, enhancement in electron conductivity can be expected due to the generation of itinerant charge carriers. At elevated temperature regimes, the excess charge carriers result from the suppression of antiferromagnetic symmetry. We observe a similar relation between σ and T for other nonstoichiometric structures. Reduction in electron conductivity can be expected with nonstoichiometry in CoO. At 300 K, σ for $V_{Co} = 4.16\%$ reduces ∼twofold to the $\sigma_{300\,K}$ of CoO. However, σ is severely suppressed with a $V_{Co} = 16.6\%$ defect density. Our calculation suggests that for $V_{Co} = 16.6\%$ at 300 K, the σ reduced $\sim 10^6$ times to $\sigma_{300\,K}$ for stoichiometric CoO. σ nearly approaches ∼0 for temperatures up to 500 K. Beyond 500 K, the enhancement in σ is observed due to the disturbance of the HS-LS spin configurations. Figure 10 explores the anisotropic behavior of the electrical conductivity at various temperatures. Below the Neel temperature (291 K), CoO does not exhibit any anisotropic behavior of its electrical conductivity. However, beyond the Neel temperature, a directional deviation is observed in the in-plane (σ_{xx}) and out-of-plane (σ_{zz}) components. The anisotropic contribution from the conduction channels of σ can be correlated to the disruption in the antiferromagnetic symmetry at elevated temperatures. Interestingly, for $V_{Co} = 4.16\%$ the component of σ starts to deviate from ∼200 K onward. σ_{zz} dominates σ_{zz}. Such anisotropic behavior can be correlated to the available energy states at the valence band near to Fermi level. Therefore, we have calculated the partial DOS of the d orbitals [49]. The DOS of d_{z^2} are dominated by the d_{xy}, d_{xz}, d_{yz} states at E_F. Therefore, we observe a higher conduction channel in σ_{xx} than σ_{zz}. At higher extent of stoichiometric disordering, an isotropic conduction ($\sigma_{xx} = \sigma_{zz}$) is observed up to ∼500 K. Both, the σ_{xx} and σ_{zz} components remain at ∼0. However, beyond 500 K, the in-plane and out-of-plane values show a distinct behavior and a rapid σ_{zz} increase. Interestingly, compared to $V_{Co} = 4.16\%$, we observe an inversion of the in-plane and out-of-plane components of σ. It is intriguing to observe that, σ_{xx} remains ∼0, even at elevated temperature regime. Severely suppressed σ_{xx} signifies that the spin blockade is operating along the in-plane direction and probably is indicating the conduction channel. A comparison to stoichiometric CoO shows that at 300 K, σ_{xx} reduces to ∼1.5 times for $V_{Co} = 4.16\%$, while we observe a drastic reduction of $\sim 10^6$ fold in σ_{xx} for $V_{Co} = 16.6\%$. Enhanced out-of-plane(σ_{zz}) conduction in $V_{Co} = 16.6\%$ can again be correlated to the available energy state of the d_{z^2} orbital. The calculated partial DOS of ($V_{Co} = 16.6\%$) exhibits the abundance population of d_{z^2} orbital states at the conduction band near E_F in the valence band, respectively [49]. However, d_{xy}, d_{xz}, d_{yz} states nearly vanish in the proximity of E_F. A distinct behavior in

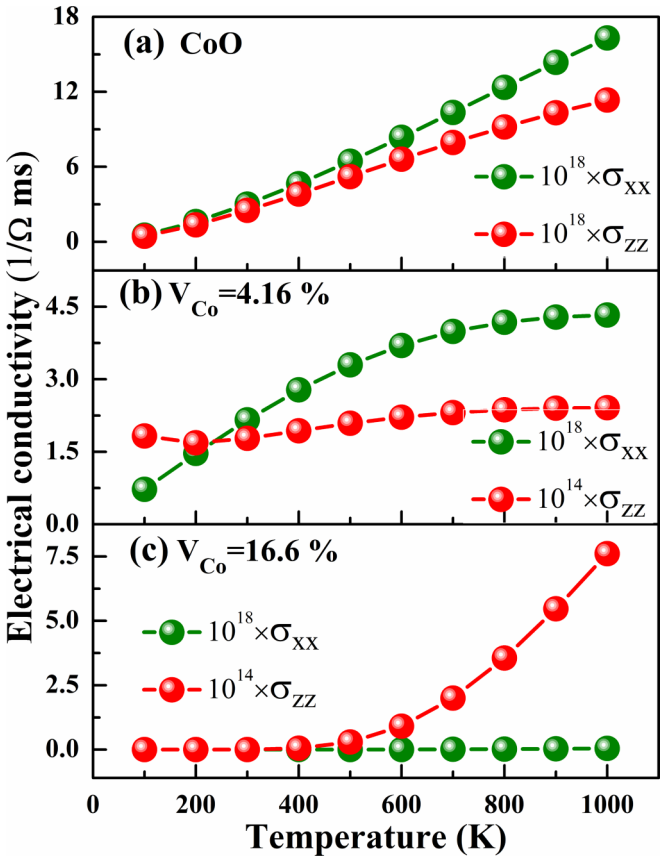

FIG. 10. Variation of anisotropic electrical conductivity as a function of temperature with a constant relaxation time ($\tau = 10^{-14}$ s) for (a) stoichiometric CoO and (b), (c) non-stoichiometric CoO, respectively. Beyond the Neel temperature, an anisotropic conductance can be observed in CoO. (c) Drastically reduced σ_{xx} ($\sigma_{xx} \sim 0$) indicates the operating spin-blockade effect along the in-plane conduction channel in $V_{Co} = 16.6\%$.

σ_{xx} and σ_{zz} at $V_{Co} = 16.6\%$ again indicates the consequence of the spin crossover.

In Sec. III A, we have computationally unveiled the spin crossover on adjacent defect atomic sites. In this section, Sec. III C, we have established the occurrence of a spin-blockade effect as a consequence of the spin crossover. Correspondingly, the computationally deduced electrical conductivity unravels a drastic reduction [$\sigma(V_{Co} = 16.6\%) \sim$ CoO $\times\ 10^{-6}$] due to the operating spin-blockade effect in nonstoichiometric CoO. Previously, a spin blockade was reported in doped cobaltates with complex stoichiometry, including heavy lanthanides, e.g., $La_{1.5}Sr_{0.5}CoO_4$, $HoBaCo_2O_{5.5}$ [72,88]. However, in the present paper, we suggest that while stabilizing the cation vacancy ordering in CoO, a spin blockade can be created in simple rock-salt CoO, via chemical pressure induced by defect engineering.

IV. CONCLUSION

In conclusion, we have computationally explored the spin-orbital-degeneracy-induced thermopower in CoO and further unraveled an operating spin-blockade effect in CoO. Ramification of the local stoichiometric disruption in CoO is a distorted octahedral crystal field and consequently a charge transfer toward a higher electronegative O atom. Resultant higher chemical pressure evokes a charge transfer to shape an additional higher charge state (Co^{+3}) on the defect adjacent atomic site. Distinct charge and spin states on subsequent atomic sites introduce a spin-orbital degeneracy in nonstoichiometric CoO, which further contributes in raising the thermal efficiency in CoO. The entropy contribution to the thermopower can further be tuned via defect engineering. Interestingly, with a higher extent of stoichiometric disordering, the ligand-field-splitting energy dominates the Hund's coupling and triggers the magnetic collapse of the Co^{+3} ion, which is located at the defect adjacent atomic site. The combination of magnetically active Co^{+2} and magnetically inert Co^{+3} on alternate atomic sites suppresses a charge hopping due to a spin-blockade effect. CoO crystalizes in the simple rock salt structure and has been well studied and characterized for decades. Yet, our present investigation unravels some unforeseen effects of defects on strong electron correlations, crystal-field splitting, and the interplay of HS-LS configuration with charge transport in CoO. Our computational study affirms that ZT_e can be tailored via defect engineering in CoO and possibly also in similar other transition-metal mono-oxides. Therefore, our present study is also compelling from an experimental perspective. The present computational investigation can further spur research interest in tailoring functional defects to explore the thermal efficiency and the spin-blockade effect in other similar TMOs.

ACKNOWLEDGMENTS

D.S. and R.A. thank Carl Tryggers Stiftelse för Vetenskaplig Forskning (CTS) for financial support. SNIC and HPC2N are acknowledged for providing the computing facilities. R.A. acknowledges financial support from Swedish Research Council (VR), Sweden. This project has received funding from the European Union's Horizon 2020 research and innovations program under Grant Agreement No. 823717-ESTEEM3.

[1] C. Gayner and K. K. Kar, Prog. Mater. Sci. **83**, 330 (2016).
[2] W. Liu, X. Yan, G. Chen, and Z. Ren, Nano Energy **1**, 42 (2012).
[3] N. Peranio, O. Eibl, S. Bäßler, K. Nielsch, B. Klobes, R. Hermann, M. Daniel, M. Albrecht, H. Görlitz, V. Pacheco *et al.*, Phys. Status Solidi A **213**, 739 (2016).
[4] W. Liu, Q. Jie, H. S. Kim, and Z. Ren, Acta Mater. **87**, 357 (2015).
[5] J. Matsuno, J. Fujioka, T. Okuda, K. Ueno, T. Mizokawa, and T. Katsufuji, Sci. Technol. Adv. Mater. **19**, 899 (2018).
[6] L. E. Bell, Science **321**, 1457 (2008).
[7] S. N. Guin, D. S. Negi, R. Datta, and K. Biswas, J. Mater. Chem. A **2**, 4324 (2014).
[8] K. Biswas, J. He, Q. Zhang, G. Wang, C. Uher, V. P. Dravid, and M. G. Kanatzidis, Nat. Chem. **3**, 160 (2011).

[9] K. Biswas, J. He, G. Wang, S.-H. Lo, C. Uher, V. P. Dravid, and M. G. Kanatzidis, Energy Environ. Sci. **4**, 4675 (2011).

[10] S. Perumal, S. Roychowdhury, D. S. Negi, R. Datta, and K. Biswas, Chem. Mater. **27**, 7171 (2015).

[11] Z. Feng, J. Zhang, Y. Yan, G. Zhang, C. Wang, C. Peng, F. Ren, Y. Wang, and Z. Cheng, Sci. Rep. **7**, 2572 (2017).

[12] J. Park, G. He, R. M. Feenstra, and A.-P. Li, Nano Lett. **13**, 3269 (2013).

[13] L. Hu, T. Zhu, X. Liu, and X. Zhao, Adv. Funct. Mater. **24**, 5211 (2014).

[14] D. Voneshen, K. Refson, E. Borissenko, M. Krisch, A. Bosak, A. Piovano, E. Cemal, M. Enderle, M. Gutmann, M. Hoesch *et al.*, Nat. Mater. **12**, 1028 (2013).

[15] M. Samanta, K. Pal, P. Pal, U. V. Waghmare, and K. Biswas, J. Am. Chem. Soc. **140**, 5866 (2018).

[16] S. Mano, T. Onimaru, S. Yamanaka, and T. Takabatake, Phys. Rev. B **84**, 214101 (2011).

[17] M. Kargarian and G. A. Fiete, Phys. Rev. B **88**, 205141 (2013).

[18] X. Xu, L. Jiang, J. Shen, Z. Chen, and Z. Xu, Phys. Lett. A **351**, 431 (2006).

[19] P. Limelette, S. Hébert, V. Hardy, R. Frésard, C. Simon, and A. Maignan, Phys. Rev. Lett. **97**, 046601 (2006).

[20] G. Tang, X. Xu, C. Tang, Z. Wang, Y. He, L. Qiu, L. Lv, L. Xing, and Y. Du, Europhys. Lett. **91**, 17002 (2010).

[21] Y. Pei, X. Shi, A. LaLonde, H. Wang, L. Chen, and G. J. Snyder, Nature (London) **473**, 66 (2011).

[22] A. Banik, T. Ghosh, R. Arora, M. Dutta, J. Pandey, S. Acharya, A. Soni, U. V. Waghmare, and K. Biswas, Energy Environ. Sci. **12**, 589 (2019).

[23] F. Guo, B. Cui, Y. Liu, X. Meng, J. Cao, Y. Zhang, R. He, W. Liu, H. Wu, S. J. Pennycook *et al.*, Small **14**, 1802615 (2018).

[24] S. N. Guin and K. Biswas, Chem. Mater. **25**, 3225 (2013).

[25] L.-D. Zhao, S.-H. Lo, Y. Zhang, H. Sun, G. Tan, C. Uher, C. Wolverton, V. P. Dravid, and M. G. Kanatzidis, Nature (London) **508**, 373 (2014).

[26] S. Fujii, M. Yoshiya, and C. A. Fisher, Sci. Rep. **8**, 11152 (2018).

[27] J. He and T. M. Tritt, Science **357**, eaak9997 (2017).

[28] S. Walia, S. Balendhran, H. Nili, S. Zhuiykov, G. Rosengarten, Q. H. Wang, M. Bhaskaran, S. Sriram, M. S. Strano, and K. Kalantar-zadeh, Prog. Mater. Sci. **58**, 1443 (2013).

[29] W. Koshibae, K. Tsutsui, and S. Maekawa, Phys. Rev. B **62**, 6869 (2000).

[30] Y. Wang, N. S. Rogado, R. Cava, and N. Ong, Nature (London) **423**, 425 (2003).

[31] J. Mravlje and A. Georges, Phys. Rev. Lett. **117**, 036401 (2016).

[32] D. Zhang, H. Guo, T. Yang, L. Qiu, Z. Wang, Y. Dai, Z. Zhang, and Y. Du, Ceram. Int. **42**, 6296 (2016).

[33] G. Tang, F. Xu, Y. He, L. Wang, L. Qiu, and Z. Wang, Phys. Status Solidi B **250**, 1327 (2013).

[34] H. Takahashi, S. Ishiwata, R. Okazaki, Y. Yasui, and I. Terasaki, Phys. Rev. B **98**, 024405 (2018).

[35] J. Androulakis, P. Migiakis, and J. Giapintzakis, Appl. Phys. Lett. **84**, 1099 (2004).

[36] Z. Liu, H. Geng, J. Mao, J. Shuai, R. He, C. Wang, W. Cai, J. Sui, and Z. Ren, J. Mater. Chem. A **4**, 16834 (2016).

[37] X. Liu, L. Xi, W. Qiu, J. Yang, T. Zhu, X. Zhao, and W. Zhang, Adv. Electron. Mater. **2**, 1500284 (2016).

[38] G. Jiang, J. He, T. Zhu, C. Fu, X. Liu, L. Hu, and X. Zhao, Adv. Funct. Mater. **24**, 3776 (2014).

[39] S. G. Jeon, D. W. Park, H. S. Shin, H. M. Park, S. Y. Choi, S. J. Lee, J. Yu, and J. Y. Song, RSC Adv. **6**, 7791 (2016).

[40] Y. Anno, Y. Imakita, K. Takei, S. Akita, and T. Arie, 2D Mater. **4**, 025019 (2017).

[41] U. D. Wdowik and K. Parlinski, Phys. Rev. B **77**, 115110 (2008).

[42] D. S. Negi, R. Datta, and J. Rusz, J. Phys.: Condens. Matter **31**, 115602 (2019).

[43] S. V. Kalinin and N. A. Spaldin, Science **341**, 858 (2013).

[44] K. Klyukin, L. L. Tao, E. Y. Tsymbal, and V. Alexandrov, Phys. Rev. Lett. **121**, 056601 (2018).

[45] K. Schwarz, P. Blaha, and G. K. Madsen, Comput. Phys. Commun. **147**, 71 (2002).

[46] P. A. Ignatiev, N. N. Negulyaev, D. I. Bazhanov, and V. S. Stepanyuk, Phys. Rev. B **81**, 235123 (2010).

[47] J. P. Perdew, K. Burke, and M. Ernzerhof, Phys. Rev. Lett. **77**, 3865 (1996).

[48] F. Tran and P. Blaha, Phys. Rev. Lett. **102**, 226401 (2009).

[49] See Supplemental Material at http://link.aps.org/supplemental/10.1103/PhysRevB.100.144108 for electronic crystal structure, power-factor, electronic figure of merit, and band-structure calculations.

[50] G. K. Madsen and D. J. Singh, Comput. Phys. Commun. **175**, 67 (2006).

[51] C. G. Shull, W. Strauser, and E. Wollan, Phys. Rev. **83**, 333 (1951).

[52] W. Roth, Phys. Rev. **110**, 1333 (1958).

[53] D. Negi, B. Loukya, and R. Datta, Appl. Phys. Lett. **107**, 232404 (2015).

[54] D. Negi, B. Loukya, K. Dileep, R. Sahu, K. Nagaraja, N. Kumar, and R. Datta, Appl. Phys. Lett. **103**, 242407 (2013).

[55] K. P. Constant, T. O. Mason, S. J. Rothman, and J. Routbort, J. Phys. Chem. Solids **53**, 405 (1992).

[56] A. Bruck and D. Tannhauser, J. Appl. Phys. **38**, 2520 (1967).

[57] J. Osorio-Guillén, S. Lany, S. V. Barabash, and A. Zunger, Phys. Rev. B **75**, 184421 (2007).

[58] U. Wdowik and D. Legut, J. Phys. Chem. Solids **69**, 1698 (2008).

[59] J. Rueff, A. Mattila, J. Badro, G. Vankó, and A. Shukla, J. Phys.: Condens. Matter **17**, S717 (2005).

[60] A. A. Dyachenko, A. O. Shorikov, A. V. Lukoyanov, and V. I. Anisimov, JETP Lett. **96**, 56 (2012).

[61] S. Yamaguchi, Y. Okimoto, and Y. Tokura, Phys. Rev. B **55**, R8666(R) (1997).

[62] K. Berggold, M. Kriener, C. Zobel, A. Reichl, M. Reuther, R. Müller, A. Freimuth, and T. Lorenz, Phys. Rev. B **72**, 155116 (2005).

[63] P. H. T. Ngamou and N. Bahlawane, Chem. Mater. **22**, 4158 (2010).

[64] R. Asahi, J. Sugiyama, and T. Tani, Phys. Rev. B **66**, 155103 (2002).

[65] H. Liu, X. Zhao, F. Liu, Y. Song, Q. Sun, T. Zhu, and F. Wang, J. Mater. Sci. **43**, 6933 (2008).

[66] I. Terasaki, Y. Sasago, and K. Uchinokura, Phys. Rev. B **56**, R12685 (1997).

[67] G. Borchardt, K. Kowalski, J. Nowotny, M. Rekas, and W. Weppner, J. Eur. Ceram. Soc. **14**, 369 (1994).

[68] R. R. Heikes and R. W. Ure, *Thermoelectricity: Science and Engineering* (Interscience Publishers, New York, London, 1961).
[69] V. Vulchev, L. Vassilev, S. Harizanova, M. Khristov, E. Zhecheva, and R. Stoyanova, J. Phys. Chem. C **116**, 13507 (2012).
[70] A. H. Reshak, J. Chyský, and S. Azam, Int. J. Electrochem. Sci. **9**, 460 (2014).
[71] M. Faizan, H. Ullah, S. Khan, S. M. Ramay, S. A. Qaid, A. Mahmood, and M. Ali, Int. J. Mod. Phys. B **31**, 1750253 (2017).
[72] A. Maignan, V. Caignaert, B. Raveau, D. Khomskii, and G. Sawatzky, Phys. Rev. Lett. **93**, 026401 (2004).
[73] F. Lewis and N. Saunders, J. Phys. C: Solid State Phys. **6**, 2525 (1973).
[74] D. T. Morelli and G. P. Meisner, J. Appl. Phys. **77**, 3777 (1995).
[75] Y.-Y. Chin, H.-J. Lin, Z. Hu, C.-Y. Kuo, D. Mikhailova, J.-M. Lee, S.-C. Haw, S.-A. Chen, W. Schnelle, H. Ishii *et al.*, Sci. Rep. **7**, 3656 (2017).
[76] P. G. Radaelli and S.-W. Cheong, Phys. Rev. B **66**, 094408 (2002).
[77] J.-M. Chen, Y.-Y. Chin, M. Valldor, Z. Hu, J.-M. Lee, S.-C. Haw, N. Hiraoka, H. Ishii, C.-W. Pao, K.-D. Tsuei *et al.*, J. Am. Chem. Soc. **136**, 1514 (2014).
[78] D. C. Freitas, C. P. C. Medrano, D. R. Sanchez, M. N. Regueiro, J. A. Rodríguez-Velamazán, and M. A. Continentino, Phys. Rev. B **94**, 174409 (2016).
[79] A. Gulec and R. Klie, J. Appl. Phys. **116**, 233701 (2014).
[80] R. F. Klie, J. C. Zheng, Y. Zhu, M. Varela, J. Wu, and C. Leighton, Phys. Rev. Lett. **99**, 047203 (2007).
[81] A. Mattila, J.-P. Rueff, J. Badro, G. Vankó, and A. Shukla, Phys. Rev. Lett. **98**, 196404 (2007).
[82] H. Wu, Phys. Rev. B **81**, 115127 (2010).
[83] J. Wang, W. Zhang, and D. Y. Xing, Phys. Rev. B **62**, 14140 (2000).
[84] H. Wu, Phys. Rev. B **86**, 075120 (2012).
[85] M. Merz, D. Fuchs, A. Assmann, S. Uebe, H. v. Löhneysen, P. Nagel, and S. Schuppler, Phys. Rev. B **84**, 014436 (2011).
[86] H. Wu and T. Burnus, Phys. Rev. B **80**, 081105(R) (2009).
[87] L. Huang, Y. Wang, and X. Dai, Phys. Rev. B **85**, 245110 (2012).
[88] C.-F. Chang, Z. Hu, H. Wu, T. Burnus, N. Hollmann, M. Benomar, T. Lorenz, A. Tanaka, H.-J. Lin, H. Hsieh *et al.*, Phys. Rev. Lett. **102**, 116401 (2009).
[89] A. A. Taskin and Y. Ando, Phys. Rev. Lett. **95**, 176603 (2005).
[90] K. Tomiyasu, S.-I. Koyama, M. Watahiki, M. Sato, K. Nishihara, Y. Takahashi, M. Onodera, K. Iwasa, T. Nojima, H. Nojiri *et al.*, J. Phys. Soc. Jpn. **85**, 094702 (2016).
[91] B. Weber, Y. M. Tan, S. Mahapatra, T. F. Watson, H. Ryu, R. Rahman, L. C. Hollenberg, G. Klimeck, and M. Y. Simmons, Nat. Nanotechnol. **9**, 430 (2014).
[92] D. Yu, B. L. Wehrenberg, I. Yang, W. Kang, and P. Guyot-Sionnest, Appl. Phys. Lett. **88**, 072504 (2006).
[93] M. Ciorga, A. S. Sachrajda, P. Hawrylak, C. Gould, P. Zawadzki, S. Jullian, Y. Feng, and Z. Wasilewski, Phys. Rev. B **61**, R16315(R) (2000).
[94] M. Pioro-Ladriere, M. Ciorga, J. Lapointe, P. Zawadzki, M. Korkusiński, P. Hawrylak, and A. S. Sachrajda, Phys. Rev. Lett. **91**, 026803 (2003).
[95] N. Shaji, C. Simmons, M. Thalakulam, L. J. Klein, H. Qin, H. Luo, D. Savage, M. Lagally, A. Rimberg, R. Joynt *et al.*, Nat. Phys. **4**, 540 (2008).